Covariance-Based Uncertainty Analysis of the NIST Electrooptic Sampling System

Dylan F. Williams, *Fellow, IEEE*, Arkadiusz Lewandowski, *Student Member, IEEE*, Tracy S. Clement, *Senior Member, IEEE*, Jack C. M. Wang, Paul D. Hale, *Senior Member, IEEE*, Juanita M. Morgan, Darryl A. Keenan, and Andrew Dienstfrey

***Abstract*—We develop a covariance matrix describing the uncertainty of mismatch-corrected measurements performed on the National Institute of Standards and Technology's electrooptic sampling system. This formulation offers a general way of describing the uncertainties of the measurement system in both the temporal and frequency domains. We illustrate the utility of the approach with several examples, including determining the uncertainty in the temporal voltage generated by the photodiode.**

***Index Terms*—Covariance matrix, electrooptic sampling, impulse response, Jacobian, standard uncertainty, uncertainty, uncertainty propagation, variance.**

I. Introduction

We develop an uncertainty analysis for the electrooptic sampling system at the National Institute of Standards and Technology (NIST) [1]–[3] that can be used in both the time and frequency domains. We then use the system to measure the complex band-limited Fourier transform of the electrical impulse response of a fast photodiode to 110 GHz and characterize the uncertainties in the measurements. These photodiodes, when stimulated with a short optical pulse, are then capable of delivering well-characterized pulses to their electrical loads and can be used to provide traceable calibrations for light-wave component analyzers, sampling oscilloscopes, large-signal network analyzers, and other high-frequency electrical instruments.

Most previous work on the characterization of electrical impulse- or step-response waveform standards has been based entirely on temporal measurements and uncertainty analyses and only report single measurands such as pulse or transition durations [4]–[9]. In this case, the *Guide to the Expression of Uncertainty in Measurement* [10] gives explicit guidance on evaluating and expressing the uncertainty of the measurands.

However, our system measures a multivariate quantity, the complex band-limited Fourier transform of the impulse response and the reflection coefficient of a fast photodiode, and [10] does not provide any guidance on expressing the uncertainties of multivariate measurands. In [1]–[3], we reported on a complete mismatch-corrected frequency-domain photodiode characterization that includes the source impedance and point-by-point frequency-domain uncertainties derived from a Monte Carlo analysis. However, these frequency-domain uncertainties could not be used to determine the accuracy of temporal quantities.

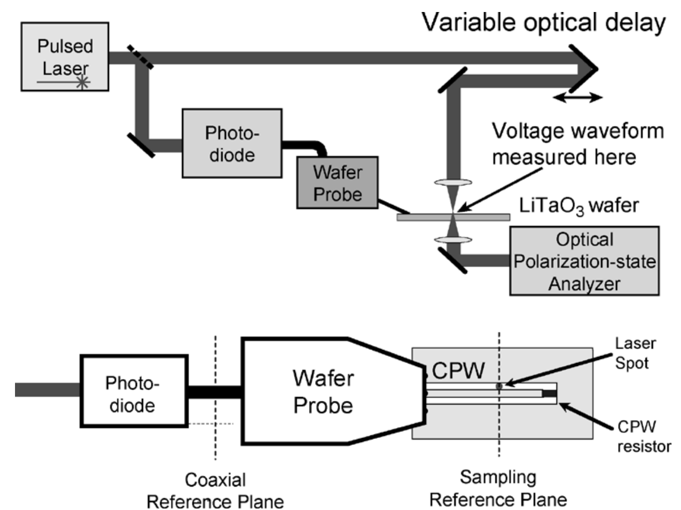

Fig. 1. Sketch of the NIST electrooptic sampling system (modeled after [1]–[3]).

Some attempts have been made to transform between temporal and frequency-domain uncertainties [11]–[17]. However, these approaches either ignored or made significant assumptions about the correlations of the errors or focus on worst case bounds, rather than uncertainty estimates.

Thus, we take a different approach in this work. Here, we use standard statistical practice to estimate the covariance matrix [18] corresponding to the multivariant quantity we report. We still provide the measured amplitude and phase of the Fourier transform of the photodiode's electrical impulse response and the measured impedance of the photodiode in the form of a reflection coefficient, thus completely characterizing the photodiode (our electrical waveform standard). However, in addition, we now also provide uncertainties on these quantities in the form of a frequency-domain covariance matrix that captures all of the correlations in the measurement uncertainties. This approach allows the uncertainty in the photodiode's electrical spectrum and impedance to be propagated through frequency-domain and temporal mismatch-corrected calibrations of other instruments. This was not possible with the approaches described previously.

II. NIST Electrooptic Sampling System

Fig. 1 sketches the NIST electrooptic sampling system. The mode-locked fiber laser emits a series of short roughly 100-fs-

Manuscript received June 29, 2005.

The authors are with the National Institute of Standards and Technology, Boulder, CO 80305 USA (e-mail: dylan@boulder.nist.gov).

Digital Object Identifier 10.1109/TMTT.2005.860492

0018-9480/$20.00 © 2006 IEEE

long optical pulses that are split by the beam splitter into an optical "excitation beam" and an optical "sampling beam." The optical excitation beam excites the photodiode, which generates a fast electrical pulse at its 1-mm connector. This is the electrical pulse that we try to characterize with the system. That electrical pulse is coupled onto the coplanar waveguide (CPW) by the wafer probe, where it is terminated by a resistive load at the end of the CPW.

We use the optical sampling beam to reconstruct the repetitive electrical waveform generated by the photodiode at the on-wafer reference plane in the CPW. We do this by passing the sampling beam through a variable optical delay, polarizing it, and then passing it through one of the gaps of the CPW. Since the $LiTaO_3$ substrate is electrooptic, the electric field between the CPW conductors changes the polarization of the optical sampling beam passing through it. We detect this change, which is proportional to the voltage in the CPW at the instant at which the optical pulse arrived there, with our polarization analyzer. By adjusting the delay in the path of the sampling beam, we adjust the relative time at which the optical pulse in the sampling beam reaches the surface of the substrate. We are thus able to trace out the voltage in the CPW as it evolves with time.

To determine the magnitude and phase of the Fourier transform of the impulse response of the photodiode, we de-embed the wafer probe from the measurements. We do this by using a frequency-domain vector network analyzer (VNA) to measure the reflection coefficients of the photodiode and CPW load and a two-tier VNA calibration to determine the scattering parameters of the wafer probe. We then transform the temporal voltage measured on the wafer into the frequency domain and translate the measurements back to the coaxial reference plane by de-embedding the probe head. This allows us to determine the voltage in the frequency domain that the photodiode would deliver to a 50-Ω load at its 1-mm coaxial port. The system and measurement procedure are described in greater detail in [1]–[3].

We use photodiodes calibrated in this way to calibrate other electrical measurement instruments. This is accomplished by stimulating the photodiode with a short optical pulse and measuring the electrical waveform the photodiode delivers to the instrument we wish to calibrate. Since the magnitude and phase of the complex Fourier transform of the photodiode's electrical impulse response and impedance are known, we can correct for imperfections in the instrument by comparing what the instrument measures to the voltage that the photodiode should have delivered to it.

III. Solution Vector

We determine the response of the photodiode with our electrooptic sampling system at the frequencies $f_i = 0, 200\ \text{MHz}, 400\ \text{MHz}, \ldots, 110\ \text{GHz}$, where $i = 0, 1, \ldots, N$ and $N = 550$. We then express the photodiode's electrical behavior in terms of the vector $\mathbf{v}$ of frequency-domain voltages v_i that the photodiode will deliver to a perfect 50-Ω load at the frequency f_i at its coaxial port when excited by a short optical pulse that generates a picocoulomb of charge at its bias port, and the vector $\mathbf{\Gamma}$ of photodiode's reflection coefficients Γ_i at its coaxial port. Since our electrooptic sampling system is not set up to measure the absolute time delay through the photodiode, we remove the linear slope of the phase response.

The resulting two complex vectors $\mathbf{v}$ and $\mathbf{\Gamma}$ offer a convenient and complete frequency-domain description of the electrical behavior of the photodiode at its coaxial port when it is used as a standard electrical source to calibrate electrical instrumentation, including high-speed sampling oscilloscopes. These quantities can also be used to derive the photodiode's Thévenin or Norton equivalent circuits [2].

We arrange these frequency-domain voltages $\mathbf{v}$ and reflection coefficients $\mathbf{\Gamma}$ in a single one-dimensional (1-D) solution vector $\mathbf{U}$ with $4(N+1)$ real elements given by

$$\mathbf{U} = \begin{bmatrix} \mathrm{Re}(\mathbf{v}) \\ \mathrm{Im}(\mathbf{v}) \\ \mathrm{Re}(\mathbf{\Gamma}) \\ \mathrm{Im}(\mathbf{\Gamma}) \end{bmatrix} \tag{1}$$

where

$$\mathrm{Re}(\mathbf{v}) = \begin{bmatrix} \mathrm{Re}(v_0) \\ \mathrm{Re}(v_1) \\ \vdots \\ \mathrm{Re}(v_N) \end{bmatrix} \quad \mathrm{Im}(\mathbf{v}) = \begin{bmatrix} \mathrm{Im}(v_0) \\ \mathrm{Im}(v_1) \\ \vdots \\ \mathrm{Im}(v_N) \end{bmatrix} \tag{2}$$

and

$$\mathrm{Re}(\mathbf{\Gamma}) = \begin{bmatrix} \mathrm{Re}(\Gamma_0) \\ \mathrm{Re}(\Gamma_1) \\ \vdots \\ \mathrm{Re}(\Gamma_N) \end{bmatrix} \quad \mathrm{Im}(\mathbf{\Gamma}) = \begin{bmatrix} \mathrm{Im}(\Gamma_0) \\ \mathrm{Im}(\Gamma_1) \\ \vdots \\ \mathrm{Im}(\Gamma_N) \end{bmatrix}. \tag{3}$$

The elements of the vector $\mathbf{U}$ contain a complete frequency-domain description of the impulse response and impedance of the photodiode to 110 GHz.

IV. Covariance Matrix $\sum_{\mathbf{U}}$ of $\mathbf{U}$

The variance of a single scalar measurand quantifies the uncertainty in its measured value. Likewise, a covariance matrix can be used to express the uncertainty of a vector quantity [18]–[22]. Here, we express the uncertainty of our voltage and reflection-coefficient measurements with the covariance matrix $\sum_{\mathbf{U}}$ of our solution vector $\mathbf{U}$, where $\mathbf{U} = [u_0, u_1, \ldots, u_{4(N+1)-1}]^{\top}$, and the superscript $\top$ indicates the transpose.

The covariance matrix $\sum_{\mathbf{U}}$ is defined by (4) [18]–[22], as shown at the bottom of this page, where $E(q)$ is the "expected value" of q and is defined by

$$E(q) = \int_{-\infty}^{\infty} qp(q)\mathrm{d}q \quad (5)$$

where $p(q)$ is the probability density function of q [19], [20].

The ith diagonal element $E((u_i - E(u_i))^2)$ of $\sum_{\mathbf{U}}$ is the variance of u_i. The square root of this variance is the standard deviation σ_i of u_i. The sample estimate of σ_i is the standard uncertainty s_i.

The ijth element of $\sum_{\mathbf{U}}$ is the covariance $\mathrm{cov}(u_i, u_j) = E((u_i - E(u_i))(u_j - E(u_j)))$ of u_i and u_j. The covariance of u_i and u_j is equal to $\sigma_i\sigma_j\rho_{ij}$, where ρ_{ij} is the correlation coefficient of u_i and u_j and satisfies $-1 \le \rho_{ij} \le 1$. The sample estimate of $\sigma_i\sigma_j\rho_{ij}$ is $s_i s_j r_{ij}$. Thus, we see that $\sum_{\mathbf{U}}$ is rich with information: it contains the variance of each of the elements of $\mathbf{U}$ and all of the correlations between each of the elements of $\mathbf{U}$.

V. Uncertainty Propagation

To fix ideas, we will now summarize the rules for uncertainty propagation with covariance matrices. These rules are treated briefly in [10], and in greater detail in [18]. We begin with a random vector $\mathbf{X}$ with mean $\mathbf{X}_0$, and a vector $\mathbf{Y}$ that is a continuous and differentiable function F of $\mathbf{X}$ around the solution $\mathbf{Y}_0 = F(\mathbf{X}_0)$. We can approximate $F(\mathbf{X})$ around $\mathbf{X}_0$ to first order with

$$\mathbf{Y} = F(\mathbf{X}) \approx F(\mathbf{X}_0) + \mathbf{J} \cdot (\mathbf{X} - \mathbf{X}_0) + \cdots \quad (6)$$

where the ijth element J_{ij} of the Jacobian $\mathbf{J}$ of F is given by

$$J_{ij} = \left.\frac{\partial F_i(\mathbf{X})}{\partial x_j}\right|_{\mathbf{X}_0} = \left.\frac{\partial y_i}{\partial x_j}\right|_{\mathbf{X}_0}. \quad (7)$$

Now we can estimate to first order the covariance matrix $\sum_{\mathbf{Y}}$ of $\mathbf{Y}$ from

$$\begin{aligned}\Sigma_{\mathbf{Y}} &\approx E\left((\mathbf{Y} - \mathbf{Y}_0)(\mathbf{Y} - \mathbf{Y}_0)^{\mathsf{T}}\right) \\ &\approx E\left(\mathbf{J}(\mathbf{X} - \mathbf{X}_0)\left(\mathbf{J}(\mathbf{X} - \mathbf{X}_0)\right)^{\mathsf{T}}\right) \\ &\approx \mathbf{J}\Sigma_{\mathbf{X}}\mathbf{J}^{\mathsf{T}}. \end{aligned} \quad (8)$$

This is an extremely powerful result, as (8) shows how the uncertainty in the independent vector $\mathbf{X}$ captured in its covariance matrix $\sum_{\mathbf{X}}$ can be propagated through complicated functions F to determine the uncertainty in the dependent vector $\mathbf{Y}$, as expressed in its covariance matrix $\sum_{\mathbf{Y}}$.

When F is linear, (6) and (8) are exact. However, when F is not linear, (8) applies only when the size of $\mathbf{X} - \mathbf{X}_0$, as captured in $\sum_{\mathbf{X}}$, is sufficiently small that (6) holds. Thus, when higher order terms in (6) dominate, as might occur near a critical point of F, (8) can fail. In our analyses, we regularly check our dominant sources of error to ensure that a higher order analysis is not required. We also used numerical Monte Carlo simulations to confirm the calculations we present in this paper.

Sometimes it is easy to evaluate the Jacobian $\mathbf{J}$ of F by analytically differentiating F. However, the functions we are interested in are often based on numerical algorithms or are too complicated to easily find $\mathbf{J}$ analytically. Thus, in practice, it is usually easier to numerically approximate $\mathbf{J}$ with finite-difference approximations. That is, it is often convenient to approximate the jth column $\mathbf{J}_{.j}$ of $\mathbf{J}$ with

$$\mathbf{J}_{\bullet j} = \frac{F(\mathbf{X} + \Delta_j) - F(\mathbf{X})}{\delta} \quad (9)$$

where the jth element of the vector Δ_j is equal to δ, δ is small, and all of the other elements of the vector Δ_j are zero. Because we use $\mathbf{J}$ only to propagate uncertainties, this first-order approximation to $\mathbf{J}$ is usually adequate.

Here, we see another powerful advantage to using a covariance-based description of the uncertainty in a vector: we can use (8) and (9) to propagate uncertainties in $\mathbf{X}$ through both analytically *and* numerically defined functions, as long as the functions are continuous and differentiable around the solution, and the errors themselves are small. We discuss an alternative form of these rules in Appendix I.

VI. Constructing $\sum_{\mathbf{U}}$

We set the solution vector $\mathbf{U}$ equal to the mean of $K = 14$ repeated measurements $\mathbf{U}_k$ of the our photodiode. We constructed the covariance matrix $\sum_{\mathbf{U}}$ of $\mathbf{U}$ from estimates of our systematic and random uncertainties. Thus, for each of these repeated measurements, we constructed a covariance matrix $\sum_{\mathbf{S}k}$ describing the systematic errors in that particular measurement. We also constructed a covariance matrix $\sum_{\mathbf{r}}$ describing the random errors, which manifest themselves as differences in our repeated measurements $\mathbf{U}_k$. Then, we combined the results to estimate the total uncertainty in our mean $\mathbf{U}$.

A. Systematic Uncertainty

We constructed the covariance matrices $\sum_{\mathbf{S}k}$ describing the systematic uncertainties in our measurements from an analysis of the impact of each of the physical error mechanisms in our electrooptic sampling system on $\mathbf{U}_k$. That is, we constructed a calibration algorithm $G(\mathbf{P}_k, \mathbf{M}_k)$ for the electrooptic sampling system that maps the raw measurements $\mathbf{M}_k$ we perform into

$$\Sigma_{\mathbf{u}} = \begin{bmatrix} E\left((u_0 - E(u_0))^2\right) & E\left((u_0 - E(u_0))(u_1 - E(u_1))\right) & \cdots \\ E\left((u_1 - E(u_1))(u_0 - E(u_0))\right) & E\left((u_1 - E(u_1))^2\right) & \cdots \\ \vdots & \vdots & \ddots \end{bmatrix} \quad (4)$$

the vector $\mathbf{U}_k = G(\mathbf{P}_k, \mathbf{M}_k)$ characterizing the photodiode's response. Here, each element of $\mathbf{P}_k$ is a parameter describing an independent physical error mechanism in the electrooptic sampling system. Then, using the finite difference formula of (9), we formed the Jacobian of G numerically and used it to map the covariance matrix $\sum_{\mathbf{P}k}$ describing the uncertainties in $\mathbf{P}_k$ into the covariance matrix $\sum_{\mathbf{S}k}$ describing the uncertainties in $\mathbf{U}_k$.

Since each of the elements of $\mathbf{P}_k$ corresponds to an independent source of error, the off-diagonal elements of $\sum_{\mathbf{P}k}$ vanish. Furthermore, the diagonal elements of $\sum_{\mathbf{P}k}$ are just the variances of the elements of $\mathbf{P}_k$, which we can determine directly from measurements or other considerations.

For example, as part of the calibration process, we measure the dc resistance of the CPW load. This dc resistance plays an important role in setting the reference impedance of the on-wafer CPW calibration and effects the results of the measurement at all frequencies.

Thus, we assigned one of the elements of $\mathbf{P}_k$ to this dc resistance and determined the value of the corresponding diagonal element of $\sum_{\mathbf{P}k}$ from the variance of this dc resistance. In this case, we determined this variance by monitoring the repeatability of our dc resistance measurements, as described in [23].

Then, we constructed the column of the Jacobian associated with this dc resistance from (9). We did this by changing the resistance value in $\mathbf{P}_k$, calculating a perturbed solution vector, and subtracting the nominal solution vector $\mathbf{U}_k$ from the perturbed solution vector, as is required in (9).

Repeating this procedure for each element in $\mathbf{P}_k$, we were able to construct, column by column, the complete Jacobian $\mathbf{J}$ mapping errors in $\mathbf{P}_k$ into $\mathbf{U}_k$. Then, we calculated $\sum_{\mathbf{S}k}$ for each measurement from $\sum_{\mathbf{S}k} = \mathbf{J} \sum_{\mathbf{P}k} \mathbf{J}^{\top}$. To simplify the calculations and bookkeeping, we set δ in (9) equal to the standard uncertainty of the corresponding elements of $\mathbf{P}_k$, and then cancelled δ out of the product $\mathbf{J} \sum_{\mathbf{P}k} \mathbf{J}^{\top}$.

We assigned an element in $\mathbf{P}_k$ to account for each of the independent physical error mechanisms discussed in [23], except for those due to the coaxial short-open-load-thru (SOLT) calibration, which we handled separately. The error mechanisms discussed in [23] that we accounted for in this way included the following:

- the finite response time of the electrooptic effect in the $LiTaO_3$ substrate;
- the finite temporal duration of the optical pulse;
- the finite optical-beam waist near the focal point of the microscope at the surface of the $LiTaO_3$ substrate;
- penetration and spatial variation of the electric field in the $LiTaO_3$ substrate below the CPW;
- multiple optical reflections in the substrate;
- variation of probe contact resistances in our dc resistance measurements;
- the accuracy with which we can position the optical beam on the wafer;
- VNA drift measured using the calibration comparison method of [24] during the CPW scattering-parameter measurements;
- error in the determination of the capacitance per unit length of the CPW;
- uncertainty in the widths and lengths of the CPW;
- asymmetry in the CPW reflect;
- metal nonuniformity in the CPW.

In each of these cases, we used the variances prescribed in [23] to set the diagonal elements of $\sum_{\mathbf{P}k}$.

We were unable to adapt the analysis of the uncertainties in the coaxial SOLT calibration used in [23] to the construction of a covariance matrix. This is because, unlike all of the other errors discussed in [23], the uncertainty analysis of the coaxial SOLT calibration used in [23] was not based on an identifiable set of independent physical mechanisms. Thus, instead of using the analysis of [23], we developed a new VNA calibration and uncertainty analysis compatible with our approach.

We designed our new VNA calibration around the calibration algorithm described in [25] and four well-characterized offset shorts and a single thru connection. This greatly simplified the associated uncertainty analysis as we were able to find well-documented mechanical uncertainties for these standards in [26] and [27].

However, our VNA calibration based on the four shorts and the thru did not perform well at low frequencies, where the difference in the reflection coefficients of the shorts becomes small. To improve the accuracy of the VNA calibration at low frequencies, we developed a two-step calibration procedure. In the first step of the calibration procedure, we developed rational-function models for the impedance of an open and a nominal 50-Ω load termination based on our band-limited calibration using the four shorts and the thru standard and the measured dc resistance of the load. In the second step of the VNA calibration procedure, we used the four shorts, the thru, and, at low frequencies, the characterized open and load terminations, as calibration standards.

To integrate our VNA error analysis into the overall analysis, we now proceed as before, assigning elements to $\mathbf{P}_k$ to account for each of the physical error mechanisms characterizing the four shorts and the thru standard. These elements accounted for the following:

- uncertainty in the lengths of our coaxial shorts;
- uncertainty in the inner and outer diameters of our shorts;
- uncertainty in pin depth;
- uncertainty in the conductor loss of the shorts;
- dc joint resistance in the test ports and standards;
- uncertainty in the measurement of the dc resistance of the load termination, which we used as a fitting parameter in the development of the rational function fit to the load;
- VNA drift measured with the calibration comparison method of [24].

Since errors in the shorts and thru standards effect both the rational function fit and the final calibration, we introduced the errors from each physical source in both the rational function fit and the final calibration, preserving the correlations between them.

Table I summarizes the magnitudes of the worst case deviations of each physical error mechanism we accounted for in this

TABLE I
PHYSICAL ERROR MECHANISMS AND THEIR WORST CASE UNCERTAINTIES IN THE 1-mm COAXIAL CALIBRATION

Physical error mechanism	Worst-case uncertainty	Source of the estimate
Short length	± 0.008 mm	[26]
Short inner diameter	± 0.003 mm	[26;27]
Short outer diameter	± 0.005 mm	[26;27]
Pin depth	± 0.005 mm	[26;27]
Individual short loss	±0. 74 GΩ/s	Type B (estimated)
Overall short loss	±7.4 GΩ/s	" "
Joint DC resistance	±0.0048 Ω	Type A (measured)
Female load DC resistance	±0.022 Ω	" "
Male load DC resistance	±0.012 Ω	" "

way. We assumed a rectangular distribution for each of the physical error mechanisms listed in the table and, in accordance with the recommendations in [28], calculated the associated variance for the quantity as one third of the square of the worst case uncertainty listed in the table.

B. Random Uncertainty

Following the recommendations in [10], we estimated the ijth element of the covariance matrix $\sum_{\mathbf{r}}$ describing our random measurement errors from

$$\Sigma_{\mathbf{r}ij} = \frac{1}{K-1}\sum_{k=1}^{K}((u_{ki}-u_i)(u_{kj}-u_j)) \tag{10}$$

where u_{ki} is the ith element of $\mathbf{U}_k$, which is the solution vector for the kth measurement of the photodiode. Here $u_i = (1/K)\sum_{k=1}^{K} u_{ki}$ is the ith element of $\mathbf{U}$, which is the mean of the K solution vectors.

We have not yet had the opportunity to perform a full analysis of the reproducibility errors in our measurements introduced by differences in wafers, probes, and scattering-parameter calibrations. However, in the course of these 14 measurements, we did use two different probe heads and four different SOLT and CPW calibrations. While mixing and matching different measurement conditions like this is not a statistically optimal way of incorporating variation due to these differences in the experimental setup into our uncertainty analysis, the random measurement errors we calculate do account for at least some of these long-term reproducibility mechanisms.

C. Total Uncertainty

Finally, we estimated the covariance matrix $\sum_{\mathbf{U}}$ of $\mathbf{U}$ with

$$\Sigma_{\mathbf{U}} = \frac{1}{K}\sum_{k=1}^{K}(\Sigma_{\mathbf{S}k}) + \frac{1}{K}\Sigma_{\mathbf{r}}. \tag{11}$$

The first term in (11) is the mean of the covariance matrices $\sum_{\mathbf{S}k}$ describing the systematic uncertainty in each of the K measurements. Because the systematic errors captured by $\sum_{\mathbf{S}k}$ do not change very much from one measurement to another, we see that the first term in (11) will not change significantly as we increase the number of measurements K.

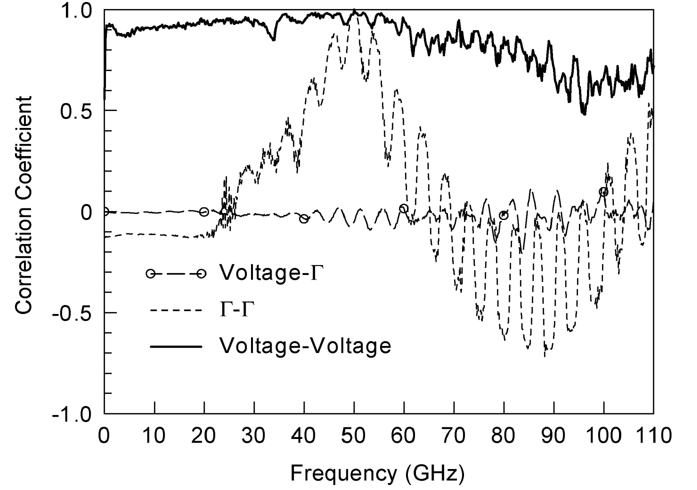

Fig. 2. Correlations between the real parts of $\mathbf{V}$ and $\mathbf{\Gamma}$ at 50 GHz and the real parts of $\mathbf{V}$ and $\mathbf{\Gamma}$ at the frequency on the horizontal axis.

The second term in (11) is the estimate of the covariance matrix describing the effect of the random differences in $\mathbf{U}$, which is the mean of the measurements. The term $1/K$ in the second term accounts for the fact that we are interested in the uncertainty in the mean solution vector $\mathbf{U}$ derived from the K measurements $\mathbf{U}_k$, rather than the uncertainty in the measurements $\mathbf{U}_k$ themselves. This term decreases as we increase the number of measurements K.

D. Correlations

Fig. 2 plots some typical correlation coefficients relating the real elements of $\mathbf{U}$ as a function of frequency. The figure shows that the covariance matrix $\sum_{\mathbf{U}}$ is dense and that the correlation coefficients are generally large. In Section VIII, we will illustrate the importance of maintaining the correlations captured in the covariance matrix $\sum_{\mathbf{U}}$ with some examples.

VII. CONFIDENCE INTERVALS AND REGIONS

We can now transform $\mathbf{U}$ and its covariance matrix $\sum_{\mathbf{U}}$ through various functions and their Jacobians to derive a variety of resultant vectors $\mathbf{Y}$ and associated covariance matrices $\sum_{\mathbf{Y}}$. Then, if the dimension p of $\mathbf{Y}$ is not too large, we can determine confidence regions for $\mathbf{Y}$.

We will usually be interested in "one-at-a-time" confidence intervals on single variables such as the magnitude or phase of a quantity at a particular frequency, a voltage at a particular point in time, or a transition or pulse duration. In this case, $\mathbf{Y}$ has a dimension $p = 1$, and $\sum_{\mathbf{Y}}$ has only one element, which is the variance of the single element of $\mathbf{Y}$.

We only used K measurements to build $\sum_{\mathbf{r}}$. Under the conservative assumption that the uncertainties captured in $\sum_{\mathbf{U}}$ are dominated by those in $\sum_{\mathbf{r}}$, we assign the number of degrees of freedom ν of $\sum_{\mathbf{Y}}$ to $K - p = K - 1$ [18]. This assumption is conservative because the $\sum_{\mathbf{S}k}$'s were built numerically and have an infinite number of degrees of freedom. Thus, it is possible, in fact, that the uncertainties in the $\sum_{\mathbf{S}k}$ dominate, and

$\sum_{\mathbf{Y}}$ actually has infinite degrees of freedom, rather than $K-1$ degrees of freedom.

Now, setting the number of degrees of freedom ν of $\sum_{\mathbf{Y}}$ to $K-1$, we can use the standard tables and practices recommended in [10] and [28] for calculating and expressing expanded uncertainties and confidence intervals.

When $\mathbf{Y}$ is multidimensional, we use a similar procedure to develop confidence regions (as opposed to intervals) for the elements of $\mathbf{Y}$. If $\mathbf{Y}'$ is the expected value of $\mathbf{Y}$, the probability that

$$(\mathbf{Y}-\mathbf{Y}')\Sigma_{\mathbf{Y}}^{-1}(\mathbf{Y}-\mathbf{Y}') \leq \frac{p}{\nu}F_{1-\alpha,p,\nu} \tag{12}$$

is $1-\alpha$, where $\mathbf{F}_{1-\alpha,p,\nu}$ is the $1-\alpha$ quantile of the F distribution with p and ν degrees of freedom [18]. Following the conservative assignment of the number of degrees of freedom we used above, we can set ν to $K-p$ in (12).

The confidence region described by (12) describes a multidimensional elliptical region in which we expect $\mathbf{Y}'$ to lie. Note that, as the number of dimensions p of $\mathbf{Y}$ increases, the requirement represented by (12) becomes more and more stringent, as we are requiring that all p elements of $\mathbf{Y}$ simultaneously lie within the region described by (12). As p approaches K, the size of this multidimensional confidence region grows infinite. This is a consequence of the limited information on correlations in $\sum_{\mathbf{Y}}$ that we captured from the finite set of measurements that we used to estimate $\sum_{\mathbf{r}}$. When $p \geq K$, the number of degrees of freedom ν becomes meaningless, and we can no longer state confidence regions for $\mathbf{Y}$.

While we can state one-at-a-time confidence intervals for the individual elements of $\mathbf{U}$, the previous discussion implies that, because $4(N+1) > K$, we cannot develop a $4(N+1)$-dimensional confidence region for the entire vector $\mathbf{U}$. Rather, we must be content with our ability to state uncertainty limits and regions for mappings of $\mathbf{U}$ onto vectors $\mathbf{Y}$ that have much lower dimensionality. This is a fundamental limitation of our measurement-based approach to estimating $\sum_{\mathbf{r}}$.

Finally, due to the small sample size used to construct $\sum_{\mathbf{r}}$, we do not claim that $\sum_{\mathbf{r}}$ (or $\sum_{\mathbf{U}}$) are reliable estimates of the true covariance matrices that may be underlying our data. That would require the order of $((4(N+1))^2$ measurements and is beyond our measurement capability. This problem is commonly encountered in finance, biology, and meteorology [29]–[31].

Principal-component analysis offers one approach to extracting underlying correlations from limited data in a systematic manner [32]. However, this is far beyond the scope of this work.

VIII. Examples

The covariance matrix $\sum_{\mathbf{U}}$ contains a wealth of uncertainty information. Furthermore, the rules in Section V for propagating covariance matrices through complicated functions of $\mathbf{U}$ give us a powerful tool for propagating the uncertainties in our photodiode measurements through a variety of instrument calibrations. We will look at a few simple examples that illustrate how to use $\sum_{\mathbf{U}}$ to propagate and evaluate the one-at-a-time uncertainties of quantities derived from $\mathbf{U}$, including temporal responses.

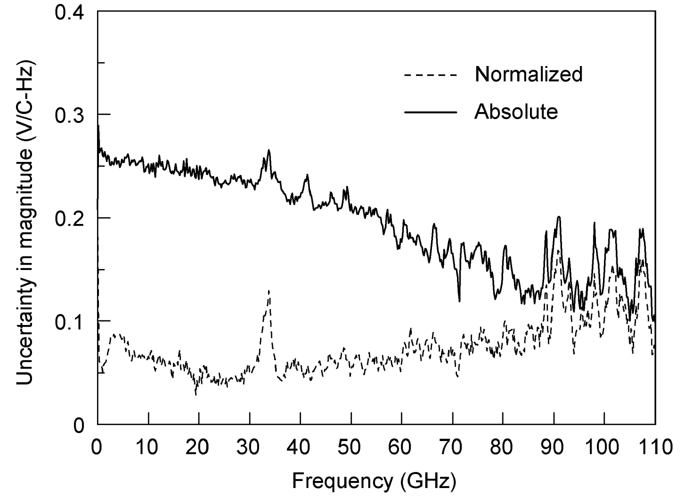

Fig. 3. Absolute and normalized standard uncertainties of the magnitude of the frequency-domain spectrum of the voltage our photodiode generates across a perfect 50-Ω load when the photodiode is excited by a short optical pulse that generates a picocoulomb of charge at its bias port.

A. Uncertainty in the Magnitude of the Elements of $\mathbf{v}$

As a first exercise, let us find the uncertainty in the magnitudes of the complex voltages in $\mathbf{v}$ from $\sum_{\mathbf{U}}$. In this case,

$$y_i = \sqrt{u_i^2 + u_{i+N+1}^2} \tag{13}$$

where $i = 0, 1, \ldots, N$. We can differentiate (13) analytically to obtain

$$J_{ij} = \frac{\partial y_i}{\partial u_j} = \begin{cases} 0, & j \neq i, j \neq i+N+1 \\ \frac{u_i}{\sqrt{u_i^2+u_{i+N+1}^2}}, & j = i \\ \frac{u_{i+N+1}}{\sqrt{u_i^2+u_{i+N+1}^2}}, & j = i+N+1 \end{cases} \tag{14}$$

or we can evaluate $\mathbf{J}$ numerically with (9). Now the covariance matrix $\sum_{\mathbf{Y}}$ of $\mathbf{Y}$ is $\mathbf{J}\sum_{\mathbf{U}}\mathbf{J}^{\top}$. We can now use $\sum_{\mathbf{Y}}$ and the rules of uncertainty propagation described in Section V to the uncertainties in $\mathbf{Y}$ through further functions and signal-processing steps.

We can also determine one-at-a-time standard uncertainties and confidence intervals for the magnitude of the elements of $\mathbf{v}$. We do this by eliminating all of the rows in $\mathbf{J}$ except that row corresponding to the particular magnitude we are interested in and recalculating $\sum_{\mathbf{Y}}$. Then, the variance in $\sum_{\mathbf{Y}}$ is the variance of the particular magnitude corresponding to the remaining row of $\mathbf{J}$, and we can calculate confidence intervals on this quantity in the usual way. Fig. 3 plots the standard uncertainty in the magnitudes of $\mathbf{v}$ obtained in this way as a solid line.

B. Normalized-Magnitude Uncertainty

We can also find the uncertainty in the normalized magnitudes of the complex voltages in $\mathbf{v}$ from the covariance matrix $\sum_{\mathbf{U}}$. We first define the constant p_0 equal to the total energy in the pulse with no errors present as $p_0 = \sum_{j=0}^{2N+1} u_j^2$. Then, the

magnitude y_i (which includes measurement errors) at frequency f_i, after normalizing the total energy in the pulse to p_0, is

$$y_i = \sqrt{u_i^2 + u_{i+N+1}^2} \frac{p_0}{\sum_{j=0}^{2N+1} u_j^2}. \quad (15)$$

Note that here we treat p_0, which is the energy to which the pulse is normalized, as fixed in (15), while the term in the denominator varies as the u_j's are varied.

Fig. 3 compares the one-at-a-time standard uncertainties in the absolute and normalized magnitudes. The higher uncertainty in the absolute magnitude at low frequencies is due to overall scaling errors in the NIST electrooptic sampling system. Since these overall scaling errors are highly correlated, they have a large effect on the uncertainty in the absolute magnitude of the voltage the photodiode delivers to a load, but a smaller effect on the normalized voltage the photodiode delivers to a load.

This example illustrates the richness of the information contained in the covariance matrix, and the ease with which we can propagate uncertainties. Had we simply determined the standard deviations in the individual elements of $\mathbf{U}$, we would not have been able to calculate the uncertainty in the normalized magnitudes of the complex voltages in $\mathbf{v}$ without more information. However, since all of the first-order information on the uncertainties and correlations in the measurements are contained in the covariance matrix, the uncertainty information contained in the covariance matrix can be easily propagated to find the uncertainty of a variety of quantities derived from $\mathbf{U}$.

C. Temporal Voltage Delivered to a 50-Ω Load

The Fourier transform is another important operation that we can apply to $\mathbf{U}$. While 110 GHz of corrected bandwidth does not completely characterize the temporal voltage the photodiode generates, applying the Fourier transform to the 110 GHz of corrected data we obtain from our electrooptic sampling system nevertheless illustrates uncertainty propagation to the time domain. Furthermore, similar band-limited transforms are useful for calibrating temporal waveform measurement instrumentation, such as sampling oscilloscopes, that have bandwidths lower than 110 GHz.

To illustrate uncertainty propagation through the Fourier transform, we implemented the Fourier transform as a matrix transformation. Since the Fourier transform is linear, it is equal to its Jacobian, further simplifying uncertainty propagation through it.

Fig. 4 shows the result of applying the Fourier transform to $\mathbf{v}$ and transforming it from the frequency domain to the time domain. Since we truncated the spectrum of our photodiode at 110 GHz, the plotted quantity is equal to the actual voltage the photodiode would deliver to a perfect 50-Ω load connected to its output port after it has been convolved with the function $\sin(2\pi f_N t)/2\pi f N t$, where f_N is 110 GHz, the cutoff frequency of the photodiode's 1-mm coaxial port. This voltage is shown as the thick solid line in Fig. 4.

The thin dashed line in Fig. 4 shows the uncertainty we calculate for the temporal representation of $\mathbf{v}$ from $\sum_{\mathbf{v}}$. It is most interesting to note the peak in the uncertainty near 40 ps. As the temporal representation of $\mathbf{v}$ peaks near 40 ps, we certainly expect higher uncertainty to be associated with these large voltages than elsewhere. This illustrates the ability of the covariance matrix to capture the correlations in the uncertainty of our frequency-domain representation, and to properly map those frequency-domain uncertainties into the correct locations in time.

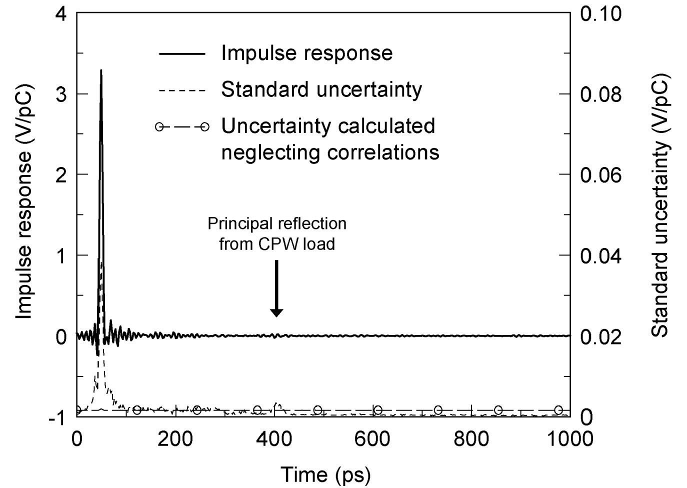

Fig. 4. Temporal voltage our photodiode generates across a perfect 50-Ω load when the photodiode is excited by a short optical pulse that generates a picocoulomb of charge at its bias port and its standard uncertainty.

The thin dashed line marked with circles in Fig. 4 illustrates the importance of including the correlations captured in the covariance matrix in calculating the uncertainty in the temporal representation of $\mathbf{v}$. It shows the uncertainty we would calculate for the temporal representation of $\mathbf{v}$ if we set the correlations in $\sum_{\mathbf{v}}$ to zero. The result of neglecting the correlations in the calculations is immense: it spreads the overall uncertainty uniformly over time, grossly underestimating the uncertainty near the main pulse at 40 ps and overestimating the uncertainty far away from the main pulse where the voltage is small.

The arrow in Fig. 4 at about 400 ps indicates the approximate point in time at which the first round-trip reflection between the photodiode and the CPW resistor occurs in our electrooptic sampling system. While the mismatch corrections we use almost entirely eliminate this artifact of the measurement system, before mismatch correction there is a residual reflection here with an amplitude of about 0.2 V/pC. The residual peak in the uncertainty we calculate from $\sum_{\mathbf{v}}$ that remains in the calibrated response near 400 ps is significant. It indicates the degree to which we are unable to correct for the multiple reflections between the photodiode and the CPW load. Of course, this residual peak in uncertainty would be missed if we were to neglect the correlations captured in $\sum_{\mathbf{v}}$, as illustrated in the figure.

D. Oscilloscope Calibration Factor

We characterized our photodiode with the NIST electrooptic sampling system to 110 GHz, the cutoff frequency of the 1-mm connectors at the photodiode's electrical output port. Thus the photodiode can be used to calibrate both frequency-domain and temporal instruments that either do not respond to frequencies

above 110 GHz or are used to measure signals whose energy is limited to frequencies below 110 GHz.

As described in Appendix II, we can use the photodiode to determine the frequency-domain magnitude and phase of the Fourier transform of the impulse response of an otherwise ideally calibrated oscilloscope that has already been corrected for time-base errors and is operating in its linear regime. Referring to Appendix II, we see that the voltage $v_s' = v_s/h$ associated with the forward wave that the photodiode delivers to the oscilloscope is given by

$$v_s' = \frac{v}{1 - \Gamma\Gamma_s}. \tag{16}$$

Here, v is the voltage in $\mathbf{v}$ that the photodiode delivers to a perfect 50-Ω load, Γ is the corresponding reflection coefficient of the photodiode in $\mathbf{\Gamma}$, and Γ_{s} is the reflection coefficient of the oscilloscope. A comparison of v_{s}, which is the voltage the oscilloscope measures, and v_{s}' allows us to determine the Fourier transform h of the impulse response of the oscilloscope to frequencies as high as 110 GHz.

We can find the uncertainty in v_{s}' due to the uncertainty in $\mathbf{U}$ by constructing the Jacobian of (16) and forming the product $\mathbf{J}\sum_{\mathbf{U}}\mathbf{J}^{\top}$ as before. The resulting covariance matrix will account not only for the error in v and Γ, but for the correlations between them. This is important, as the reflection coefficient measurements Γ are used in the corrections we employ to determine v from our electrooptic-sampling-system measurements, correlating the errors in v and Γ.

We must also account for the uncertainty due to errors in the measurement of the oscilloscope reflection coefficient Γ_{s}. Typically, Γ will be measured at NIST and Γ_{s} measured with a different calibration by the user of the photodiode, and so Γ and Γ_{s} will be uncorrelated. When Γ and Γ_{s} are uncorrelated, we can simply construct a second Jacobian mapping errors in Γ_{s} into errors in v_{s}, propagate the errors in Γ_{s} through (16), and add the resulting covariance matrix to the product $\mathbf{J}\sum_{\mathbf{U}}\mathbf{J}^{\top}$ that we calculate in the first step of the analysis. This is the standard approach.

However, this was not entirely justified in our case, as we do not currently have access to a second 1-mm calibration set at NIST. Thus, we used the same calibration set for both measurements and accounted for the correlations in Γ and Γ_{s}.

Fig. 5 shows the band-limited forward temporal voltage v_{s}' we calculate from (16) that the photodiode delivers to the oscilloscope. The principal reflection from the oscilloscope occurs at about 850 ps. This reflection is absent in Fig. 4.

The one-at-a-time uncertainties in v_{s}' we calculate from $\sum_{\mathbf{v}}$ are extremely close to those of the photodiode impulse response except near 850 ps, where the uncertainty of v_{s}' increases significantly. This increase in the temporal uncertainty of v_{s}' accounts for the inaccuracies in the measurement of the oscilloscope's reflection coefficient and reflects the degree to which we are able to correct for the principal reflection from the scope with our VNA measurements. Again, traditional approaches to uncertainty analysis that do not account for correlations in the measurements are not able to correctly map uncertainties in the frequency domain to the correct temporal locations, such as the position of this principal reflection at 850 ps. This is illustrated

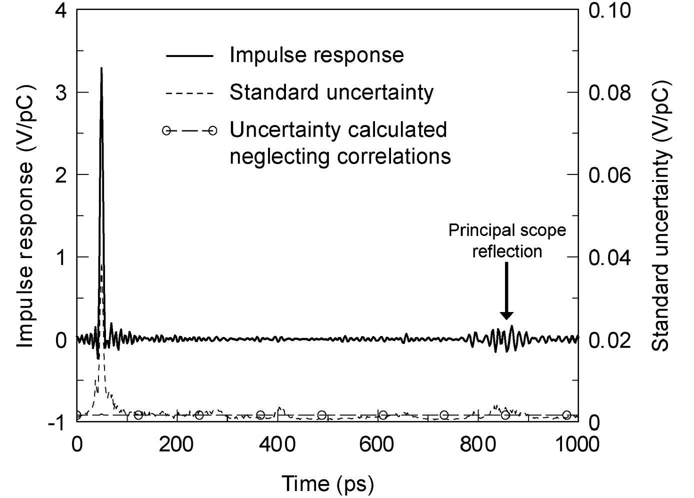

Fig. 5. Temporal voltage that our photodiode delivers to an oscilloscope when it is excited by a short optical pulse that generates a picocoulomb of charge at its bias port and its standard uncertainty.

by the curve labeled "Uncertainty calculated neglecting correlations" in Fig. 5, which shows the result of neglecting these correlations in the analysis.

IX. Conclusion

Our covariance-based description of the uncertainties of the NIST electrooptic sampling system allows greater flexibility in applying the photodiodes to instrument calibration than was previously possible. In particular, there is enough information in the covariance matrix to allow the uncertainties to be propagated through Fourier and other complex transformations to the time domain. This is exciting because this approach to representing uncertainty allows frequency-domain mismatch corrections and traceable electrooptic-sampling-system calibrations to be applied to both frequency- and time-domain instruments. This development promises to usher in a new paradigm in the way that high-frequency electrical instrumentation, and particularly high-frequency electrical instrumentation requiring mismatch correction, is calibrated.

Appendix I
Large Covariance Matrices

The covariance matrix $\sum_{\mathbf{U}}$ is quite large and exceeds the maximum size matrix available in some programming environments. To minimize the size of the matrices we must deal with, we broke the $4(N+1)$ by $4(N+1)$ matrix $\sum_{\mathbf{U}}$ up into three $N+1$ by $N+1$ equally sized submatrices $\sum_{\mathbf{v}}$, $\sum_{\mathbf{\Gamma}}$, and $\sum_{\mathbf{v\Gamma}}$ before storing them to disk. That is, we wrote $\sum_{\mathbf{U}}$ as

$$\Sigma_{\mathbf{u}} = \begin{bmatrix} \Sigma_{\mathbf{v}} & \Sigma_{\mathbf{v\Gamma}} \\ \Sigma_{\mathbf{v\Gamma}}^{\mathrm{T}} & \Sigma_{\mathbf{\Gamma}} \end{bmatrix}. \tag{17}$$

The submatrix $\sum_{\mathbf{v}}$ in (17) captures the uncertainties in $\mathbf{v}$, the submatrix $\sum_{\mathbf{\Gamma}}$ captures the uncertainties in $\mathbf{\Gamma}$, and the submatrix $\sum_{\mathbf{v\Gamma}}$ captures the correlations between $\mathbf{v}$ and $\mathbf{\Gamma}$.

To use these matrices, we can either reassemble $\sum_{\mathbf{U}}$ and use (8) directly or we can rewrite (8) as

$$\Sigma_{\mathbf{Y}} = [\mathbf{J}_{\mathbf{v}} \quad \mathbf{J}_{\mathbf{\Gamma}}] \begin{bmatrix} \Sigma_{\mathbf{v}} & \Sigma_{\mathbf{v\Gamma}} \\ \Sigma_{\mathbf{v\Gamma}}^{\mathrm{T}} & \Sigma_{\mathbf{\Gamma}} \end{bmatrix} \begin{bmatrix} \mathbf{J}_{\mathbf{v}}^{\mathrm{T}} \\ \mathbf{J}_{\mathbf{\Gamma}}^{\mathrm{T}} \end{bmatrix} \tag{18}$$

where we have split $\mathbf{J}$ into two equally sized submatrices $\mathbf{J_v}$ and $\mathbf{J_\Gamma}$ with

$$\mathbf{J} = [\mathbf{J_v} \quad \mathbf{J_\Gamma}]. \tag{19}$$

Now we can expand (18) as

$$\Sigma_\mathbf{Y} = \mathbf{J_v}\Sigma_\mathbf{v}\mathbf{J_v}^\mathsf{T} + \mathbf{J_\Gamma}\Sigma_\Gamma\mathbf{J_\Gamma}^\mathsf{T} + \mathbf{J}_\mathrm{v}\Sigma_{\mathrm{v}\Gamma}\mathbf{J}_\Gamma^\mathsf{T} + \left(\mathbf{J_v}\Sigma_{\mathbf{v}\Gamma}\mathbf{J_\Gamma}^\mathsf{T}\right)^\mathsf{T}. \tag{20}$$

Equation (20) can be useful because it limits the size of the covariance matrices that must be evaluated to solve for the covariance matrix $\sum_\mathbf{Y}$ in (8).

Appendix II
High-Speed Oscilloscope Calibration

Here, we present a derivation of (16), which determines the band-limited Fourier transform h of the impulse response of a high-speed sampling oscilloscope. These high-speed oscilloscopes offer a very convenient way of testing fast electrical components that are designed to operate in a 50-Ω electrical environment.

A. Wave Representation

It is common to use frequency-domain forward and backward wave amplitudes a and b normalized to a 50-Ω reference impedance in place of voltages and currents at microwave frequencies [33]. We use the "pseudowaves" of [33], which correspond to the conventional power-normalized forward and backward wave amplitudes with a reference impedance of 50 Ω [34]. These wave amplitudes have units of the square root of a Watt, and are conventionally normalized so that the average power p transmitted across a reference plane is given by $p = 1/2(a^2 - b^2)$.[1]

By limiting ourselves to the characterization of signals with bandwidths below the cutoff frequency of the guiding structures we use, we are able to apply frequency-domain microwave mismatch corrections developed for linear time-invariant systems to the oscilloscope calibration problem. Fig. 6 shows the microwave flow diagram describing the propagation of signals when a generator is connected directly to a high-speed sampling oscilloscope. This diagram is a simplification of the models developed in [35] and [36]. Strictly speaking, the diagram is only applicable if the generator and oscilloscope can be treated as linear time-invariant circuits. This is a reasonable approximation in our case, although the techniques used to ensure that the generator and oscilloscope can be treated this way are beyond the scope of this paper.

The generator on the left-hand-side of the diagram in Fig. 1 is characterized by its forward-wave source amplitude b_g and its reflection coefficient Γ_g. This wave-based representation of the source is equivalent to the Thévenin-equivalent-circuit and Norton-equivalent-circuit representations commonly used to describe electrical sources at lower frequencies. References [2] and [34] present formulas for converting between this wave-based representation and Thévenin and Norton equivalent circuits.

[1]Reference [1] uses a less common rms normalization in which the power p is given by $p = \underline{a}^2 - \underline{b}^2$, where $\underline{a}$ and $\underline{b}$ are the rms pseudowaves of [1]. The rms-normalized pseudowaves of [1] are related to those used here with $\underline{a} = a/\sqrt{2}$ and $\underline{b} = b/\sqrt{2}$.

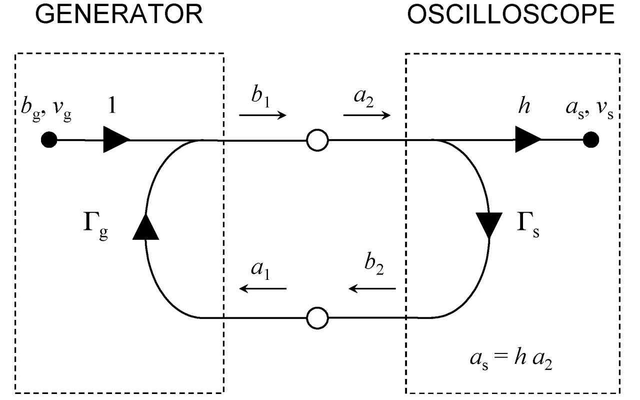

Fig. 6. Microwave flow diagram describing the propagation of signals between a generator and an oscilloscope.

The oscilloscope on the right-hand side of Fig. 1 is characterized by the Fourier transform h of its impulse response and by its reflection coefficient Γ_s.

In quasi-TEM guides with a suitable choice of voltage path, we can write the peak voltage v_g of the "forward voltage wave" associated with the wave amplitude b_g as [33]

$$v_\mathrm{g} = \sqrt{50\,\Omega}\, b_\mathrm{g}. \tag{21}$$

The square root of 50 Ω in (1) converts the power-normalized wave amplitude b_g to a peak voltage. The voltage v_g is the peak voltage that the generator would generate across a perfect 50-Ω load. It can also be thought of as the voltage that the forward wave b_g would carry with it as it propagates down a perfect 50-Ω transmission line and can be derived by setting the normalizing voltage v_0 real, the reference impedance Z_ref to 50 Ω, and the backward-wave amplitude b to zero in [33, eq. (55)].

Likewise, the relation between the peak voltage v_s that the oscilloscope measures and the wave a_s in Fig. 1 is given by

$$v_\mathrm{s} = \sqrt{50\,\Omega}\, a_\mathrm{s}. \tag{22}$$

Finally, we would like to point out that the voltage v_g should not be confused with the total voltage at the generator's output port when the impedance of the load connected to the generator is not equal to 50 Ω. This is because an imperfect load will reflect some of the energy incident on it back to the generator, and both the forward and backward waves b_1 and a_1 will then contribute to the total voltage at the generator's output port. The multiple reflections between the generator and the oscilloscope must be accounted for with a mismatch correction.

B. Mismatch Correction

We now solve for the wave amplitude a_2. This is the amplitude of the forward wave delivered to the oscilloscope by the generator. The wave amplitudes at the generator's output port are related by [33], [34]

$$b_1 = b_\mathrm{g} + \Gamma_\mathrm{g} a_1 \tag{23}$$

while the wave amplitudes at the input of the oscilloscope are related by

$$b_2 = \Gamma_\mathrm{s} a_2. \tag{24}$$

Since the generator and oscilloscope are connected directly together in Fig. 1, the voltages and currents are continuous across that junction, and $b_1 = a_2$ and $a_1 = b_2$. Thus, we can combine (23) and (24) to obtain [33], [34], [36]

$$a_2 = \frac{b_g}{1 - \Gamma_g \Gamma_s}. \tag{25}$$

Finally, the oscilloscope measures the voltage v_s given by

$$v_s = \sqrt{50\,\Omega}\, a_s = \sqrt{50\,\Omega}\, h \frac{b_g}{1 - \Gamma_g \Gamma_s} = h \frac{v_g}{1 - \Gamma_g \Gamma_s} \tag{26}$$

which reduces to (16) when the oscilloscope is excited by a photodiode. We refer to h in (26) as the complex frequency response of the oscilloscope. This frequency response is the band-limited Fourier transform of the oscilloscope's impulse response and accounts for the finite response time of the oscilloscope to the signal delivered to it by the generator. It is equal to the ratio of the voltage v_s that the oscilloscope measures and the voltage $v_2 = \sqrt{50\,\Omega} a_2$ associated with the forward wave a_2 that the generator delivers to the oscilloscope.

References

[1] T. S. Clement, P. D. Hale, D. F. Williams, and J. M. Morgan, "Calibrating photoreceiver response to 110 GHz," in *15th Annu. Meeting IEEE Lasers and Electro-Optics Sox. Conf. Dig.*, Nov. 2002, pp. 877–878.

[2] D. F. Williams, P. D. Hale, T. S. Clement, and J. M. Morgan, "Mismatch corrections for electro-optic sampling systems," in *Automatic RF Techniques Group Conf. Dig.*, vol. 56, Nov. 2000, pp. 141–145.

[3] ——, "Calibrating electro-optic sampling systems," in *IEEE MTT-S Int. Microwave Symp. Dig.*, vol. 3, May 2001, pp. 1527–1530.

[4] D. R. Larson, N. G. Paulter, and D. I. Bergman, "Pulse parameter dependence on transition occurrene instant and waveform epoch," *IEEE Trans. Instrum. Meas.*, vol. 54, no. 4, pp. 1520–1526, Aug. 2005.

[5] N. G. Paulter, A. J. A. Smith, D. R. Larson, T. M. Souders, and A. G. Roddie, "NIST-NPL interlaboratory pulse measurement comparison," *IEEE Trans. Instrum. Meas.*, vol. 52, no. 6, pp. 1825–1833, Dec. 2003.

[6] N. G. Paulter and D. R. Larson, "Sources of uncertainty in the nose-to-nose sampler calibration method," *IEEE Trans. Instrum. Meas.*, vol. 52, no. 5, pp. 1618–1626, Aug. 2003.

[7] N. G. Paulter and D. R. Larson, "Pulse parameter uncertainty analysis," *Metrologia*, vol. 39, pp. 143–155, 2002.

[8] D. Henderson, A. G. Roddie, and A. J. A. Smith, "Recent developments in the calibration of fast sampling oscilloscopes," *Proc. Inst. Elect. Eng.*, pt. A, vol. 139, no. 5, pp. 254–260, Sep. 1992.

[9] A. J. A. Smith, A. G. Roddie, and P. D. Woolliams, "Optoelectronic techniques for improved high speed electrical risetime," in *Proc. Int. Microwave Symp.*, vol. 3, Jun. 2002, pp. 1501–1504.

[10] *Guide to the Expression of Uncertainty in Measurement*, 1993.

[11] T. Daboczi, "Uncertainty of signal reconstruction in the case of jittery and noisy signals," *IEEE Trans. Instrum. Meas.*, vol. 47, no. 5, pp. 1062–1066, Aug. 1998.

[12] J. J. Blair, "Error estimates for frequency responses calculated from time-domain measurements," *IEEE Trans. Instrum. Meas.*, vol. 47, no. 2, pp. 345–353, Apr. 1998.

[13] J. P. Deyst and T. M. Souders, "Bounds in frequency response estimates derived from uncertain step response data," *IEEE Trans. Instrum. Meas.*, vol. 45, no. 2, pp. 378–383, Apr. 1996.

[14] C. J. Pritchard and B. Wigdorowitz, "On the determination of time-domain signal levels at the specification stage in quantitative feedback theory controller systhesis," *Int. J. Control*, vol. 66, no. 2, pp. 329–348, Jan. 1977.

[15] ——, "Improved method of determining time-domain transient performance bounds from frequency response uncertainty regions," *Int. J. Control*, vol. 66, no. 2, pp. 311–327, Jan. 1997.

[16] ——, "Mapping frequency response bounds to the time domain," *Int. J. Control*, vol. 64, no. 2, pp. 335–343, Jan. 1996.

[17] M. Mirshafi and J. M. Edmunds, "Mapping circular bounds on frequency responses to bounds on time responses," *Int. J. Control*, vol. 59, no. 2, pp. 473–483, Jan. 1994.

[18] F. A. Graybill, *Theory and Application of the Linear Model*. Belmont, CA: Dunbury Press, 1976.

[19] W. Mendenhall and T. Sincich, *Statistics for Engineering and the Sciences*, 3rd ed. San Francisco, CA: Dellen, 1988.

[20] S. Ross, *A First Course in Probability*. New York: Macmillan, 1976.

[21] N. M. Ridler and M. J. Salter, "Evaluating and expressing uncertainty in complex S-parameter measurements," in *Automatic RF Techniques Group Conf. Dig.*, vol. 56, Dec. 2000, pp. 63–75.

[22] ——, "Propagating S-parameter uncertainties to other measurement quantities," in *Automatic RF Techniques Group Conf. Dig.*, vol. 58, Dec. 2001, pp. 71–89.

[23] D. F. Williams, P. D. Hale, T. S. Clement, and C. M. Wang, "Uncertainty of the NIST electrooptic sampling system," NIST, Boulder, CO, NIST Tech. Note 1535, Dec. 2004.

[24] D. F. Williams, R. B. Marks, and A. Davidson, "Comparison of on-wafer calibrations," in *Automatic RF Techniques Group Conf. Dig.*, vol. 38, Dec. 1991, pp. 68–81.

[25] D. F. Williams, C. M. Wang, and U. Arz, "An optimal vector-network-analyzer calibration algorithm," *IEEE Trans. Microw. Theory Tech.*, vol. 51, no. 12, pp. 2391–2401, Dec. 2003.

[26] *Agilent Technologies 85059A 1.0 mm Precision Calibration/Verification Kit Operating and Service Manual*, vol. 85 059-90 003, Dec. 2000.

[27] K. Howell and K. Wong, "DC to 110 GHz Measurements in coax using the 1 mm connector," *Microwave J.*, pp. 22–34, Jun. 1999.

[28] B. N. Taylor and C. E. Kuyatt, "Guidelines for evaluating and expressing the uncertainty of NIST measurement results," NIST, Boulder, CO, NIST Tech. Note 1297, Sep. 1994.

[29] D. V. Nguyen and D. M. Rocke, "Tumor classification by partial least-squares using microarray gene expression data," *Bioinformatics*, vol. 18, pp. 39–50, 2002.

[30] R. W. Preisendorfer, *Principal Components Analysis in Meteorology and Oceanography*. Amsterdam, The Netherlands: North-Holland, 1988.

[31] D. Wilcox and T. Gebbie, "On the analysis of cross-correlations in South African market data," *Phys. A—Stat. Mech. and Its Applicat.*, vol. 344, no. 1, pp. 294–298, 2004.

[32] J. E. Jackson, *A User's Guide to Principal Components*. Hoboken, NJ: Wiley-Interscience, 2002.

[33] R. B. Marks and D. F. Williams, "A general waveguide circuit theory," *J. Res. Nat. Inst. Standards Technol.*, vol. 97, no. 5, pp. 533–562, 1992.

[34] D. M. Kerns and R. W. Beatty, *Basic Theory of Waveguide Junctions and Introductory Microwave Network Analysis*, 1st ed. Oxford, U.K.: Pergamon, 1967.

[35] J. Verspecht and K. Rush, "Individual characterization of broadband sampling oscilloscopes with a nose-to-nose calibration procedure," *IEEE Trans. Instrum. Meas.*, vol. 43, no. 2, pp. 347–354, Apr. 1994.

[36] D. C. DeGroot, P. D. Hale, M. Vanden Bossche, F. Verbeyst, and J. Verspecht, "Analysis of interconnection networks and mismatch in the nose-to-nose calibration," in *Automatic RF Techniques Group Conf. Dig.*, vol. 55, Jun. 2000, pp. 116–121.

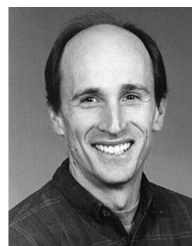

Dylan F. Williams (M'80–SM'90–F'02) received the Ph.D. degree in electrical engineering from the University of California, Berkeley, in 1986.

He joined the Electromagnetic Fields Division, National Institute of Standards and Technology, Boulder, CO, in 1989, where he develops metrology for the characterization of monolithic microwave integrated circuits and electronic interconnects. He has published over 80 technical papers.

Dr. Williams is an Associate Editor for the IEEE TRANSACTIONS ON MICROWAVE THEORY AND TECHNIQUES. He was the recipient of the Department of Commerce Bronze and Silver Medals, two Electrical Engineering Laboratory's Outstanding Paper Awards, two Automatic RF Techniques Group (ARFTG) Best Paper Awards, the ARFTG Automated Measurements Technology Award, and the IEEE Morris E. Leeds Award.

Arkadiusz Lewandowski (S'02) was born in Poland in 1975. He received the M.Sc. degree in electrical engineering and the Ph.D. degree from Warsaw University of Technology, Poland, in 2001.

In 2002, he joined Institute of Electronics Systems, Warsaw University of Technology, pursuing the Ph.D. degree in the area of microwave measurements. From 1999 to 2000, he was with the Department of High Frequency Techniques, University of Kassel, Kassel, Germany, working on the design of microwave oscillators. From 2002 to 2004, he was involved with the development of digital generators of radar signals with Telecommunications Research Institute, Warsaw, Poland. He is currently a Guest Researcher with the National Institute of Standards and Technology, Boulder, CO, where he is engaged in the development of VNA calibration methods applicable for time-domain measurements. His present research interests include on-wafer microwave measurements and VNA calibration techniques.

Mr. Lewandowski was the recipient of the 2005 IEEE Microwave Theory and Techniques Society (MTT-S) Graduate Fellowship Award, the second prize of the AP/AES/MTT Joint Chapter of Poland Section IEEE for the best M.Sc. thesis, and the second prize of EuMA for the Best Student Paper at the International Microwave Conference MIKON 2002, Poland.

Tracy S. Clement (S'89–M'92–SM'05) received the Ph.D. degree in electrical engineering from Rice University, Houston, TX, in 1993. Her Ph.D. research involved developing and studying a variety of ultrashort pulse and very short wavelength lasers.

Since 1998, she has been with the Optoelectronics Division of the National Institute of Standards and Technology (NIST), Boulder, CO. Her current research interests include the development of measurement systems for high-speed electrooptic components as well as ultrashort pulse laser measurements. Prior to joining the Optoelectronics Division, she was an Associate Fellow of JILA, the Quantum Physics Division of NIST, and was an Assistant Professor Adjoint with the Department of Physics, University of Colorado, Boulder. From 1993 to 1995, she was a Director's Postdoctoral Fellow with Los Alamos National Laboratory, Los Alamos, NM.

Jack C. M. Wang received the Ph.D. degree in statistics from Colorado State University, Fort Collins, in 1978.

He is a Mathematical Statistician with the Statistical Engineering Division of the National Institute of Standards and Technology, Boulder, CO. His research interests include interval estimation on variance components, statistical graphics and computing, and the application of statistical methods to physical sciences.

Dr. Wang is a Fellow of the American Statistical Association.

Paul D. Hale (M'01–SM'01) received the Ph.D. degree in applied physics from the Colorado School of Mines, Golden, CO, in 1989.

He has been a Staff Member of the National Institute of Standards and Technology (NIST), Boulder, CO, since 1989 and has conducted research in birefringent devices, mode-locked fiber lasers, fiber chromatic dispersion, broad-band lasers, interferometry, polarization standards, and high-speed optoelectronic measurements. He is presently Leader of the High-Speed Measurements Project in the Sources and Detectors Group. His research interests include high-speed optoelectronic and microwave measurements and their calibration.

Dr. Hale was the recipient of the Department of Commerce Bronze, Silver, and Gold awards, two ARFTG Best Paper Awards, and the NIST Electrical Engineering Laboratory's Outstanding Paper Award. He is currently an Associate Editor of the JOURNAL OF LIGHTWAVE TECHNOLOGY.

Juanita M. Morgan was born in Wellston, OH. She has held research positions at Xicor, Ball Aerospace, and Dynatech Electro-Optics. Since 1990, she has been with the Electromagnetics Division, National Institute of Standards and Technology, Boulder, CO. Her current research interests include processing of high-speed compound semiconductor devices.

Darryl A. Keenan received the B.S. degree in physics from the University of Colorado, Fort Collins, in 1996.

In 1989 he joined the National Institute of Standards and Technology (NIST, then NBS), Boulder, CO, and has since been a member of the Sources and Detectors Group of the Optoelectronics Division. He has run optical laser metrology laboratories including low-power CW from the visible to near infrared, high-power CW at far infrared, Q-switched Nd:YAG at near infrared, and Excimer at ultraviolet to deep-ultraviolet. He has worked with colleagues to develop optical fiber connector characterization and to develop a system for measuring detector nonlinearity at 193 nm. His current areas of work are in optical laser metrology at 193 and 248 nm and time- and frequency-domain characterization of oscilloscopes using Swept Sine measurements and calibrated photodiodes.

Andrew Dienstfrey received the B.A. degree in mathematics from Harvard College, Cambridge, MA, in 1990, and the Ph.D. degree in mathematics from the Courant Institute of Mathematical Sciences, New York, in 1998.

From 1998 to 2000, he was a Post-Doctoral Scientist with the Courant Institute of Mathematical Sciences, investigating methods for remote sensing of dielectric properties of superconducting thin films. He joined the Mathematical and Computational Sciences Division, National Institute of Standards and Technology, Boulder, CO, in 2000. His research interests include theoretical and computational aspects of periodic scattering problems in acoustics and electromagnetics.